

pubs.acs.org/journal/ascecg Research Article

Mass Transport Modifies the Interfacial Electrolyte to Influence Electrochemical Nitrate Reduction

Jinyu Guo, Paige Brimley, Matthew J. Liu, Elizabeth R. Corson, Carolina Muñoz, Wilson A. Smith, and William A. Tarpeh*



Cite This: ACS Sustainable Chem. Eng. 2023, 11, 7882–7893



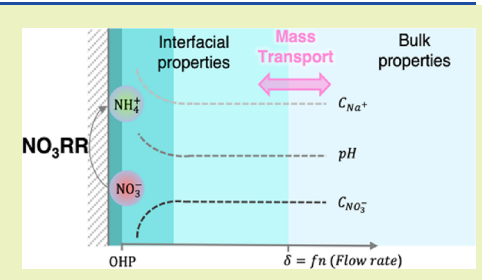
ACCESS I

Metrics & More

Article Recommendations

s Supporting Information

ABSTRACT: The electrochemical nitrate reduction reaction (NO₃RR) can facilitate remediation of nitrate-polluted wastewater and sustainable production of ammonia. As an important component of the reaction microenvironment, the interfacial electrolyte substantially influences NO₃RR but remains underexplored. Mass transport modifies the interfacial electrolyte properties (e.g., pH, solute concentrations) and thus regulates NO₃RR activity and selectivity. In a representative flow-cell configuration with a titanium NO₃RR electrode, we systematically controlled mass transport conditions and demonstrated their impacts on NO₃RR performance. With continuum model simulation and *in situ* infrared absorption



spectroscopy, we characterized the interfacial electrolyte environment under varied mass transport conditions. Furthermore, we strategically tuned the interfacial electrolyte properties and experimentally deconvoluted their impacts on NO₃RR activity and selectivity. We found that diffusion layer thickness and background electrolyte concentration govern NO₃RR activity, while interfacial pH steers NO₃RR selectivity. Inspired by these findings, we applied pulsed potential to periodically refresh the interfacial electrolyte environment and lower the local pH, successfully tripling the relative ammonia-to-nitrite selectivity. Distinct from NO₃RR studies that focus on reaction kinetics, this study was conducted under commonly observed mass transport limitations to advance mechanistic understanding behind mass transport effects and to help identify engineering opportunities that optimize ammonia production.

KEYWORDS: diffusion—migration—reaction model, electrolyte effects, infrared absorption spectroscopy, reaction microenvironment, reactive nitrogen, sustainable ammonia manufacturing

■ INTRODUCTION

Anthropogenic activities have imbalanced the global nitrogen cycle via large-scale Haber-Bosch ammonia manufacturing. The removal of reactive nitrogen species (all inorganic forms besides dinitrogen) has fallen far behind their production, leading to heavy environmental burdens and continuous losses from the nitrogen economy. As the most prevalent waterborne reactive nitrogen pollutant, excessive nitrate (NO₃⁻) jeopardizes both human and ecosystem health.¹⁻⁷ Meanwhile, the reactive nature of nitrate presents a promising opportunity to transform it into other value-added nitrogen products via the electrochemical nitrate reduction reaction (NO₃RR). One representative product is ammonia (NH₃), a widely used commodity chemical, green energy carrier, and fertilizer component. By leveraging renewable energy, electrochemical NO₃RR enables nitrate-polluted water remediation and sustainable ammonia production. Distributed electrochemical NO₃RR can reduce transportation costs embedded in traditional centralized wastewater treatment and chemical manufacturing and help address spatial and temporal imbalances in the nitrogen cycle. $^{8-10}$

In ongoing efforts to improve activity and ammonia selectivity of electrochemical NO₃RR, researchers have mainly

focused on improving electrocatalysts. However, it has been increasingly recognized that the reaction microenvironment, which contains both the electrocatalyst and the interfacial electrolyte between the electrocatalyst and the bulk electrolyte, directly influences electrocatalytic reduction reactions (e.g., carbon dioxide reduction reaction, CO₂RR; oxygen reduction reaction, ORR; hydrogen evolution reaction, HER). ^{11–20} Specifically, the interfacial electrolyte is composed of a compact electrical double layer (EDL) that extends a few nanometers away from the electrode surface and a diffusion layer that spans up to a few hundred microns into the bulk electrolyte. ²¹ As the immediate environment where reactions take place, the interfacial electrolyte physicochemical properties (e.g., electric potential, pH, solute concentrations) may differ drastically from the bulk. ^{11,17,22} Among these properties, electric potential serves as the thermodynamic driving force for

Received: February 22, 2023 Revised: April 10, 2023 Published: May 6, 2023





electrode reactions, and pH indicates the abundance of proton sources, both of which influence reaction activity and selectivity. In terms of ionic solutes, coexisting anions (e.g., Cl^{-} , SO_4^{2-}) can compete with reactant nitrate for surface sites and affect activity; cations (e.g., Na+, K+) are known to interact with reaction intermediates as well as modify the interfacial electric field and pH, thus influencing activity and selectivity. 13,23,24 Although the effects of bulk electrolyte properties on electrochemical NO3RR have been reported, 5,25-27 few studies have explicitly investigated the interfacial electrolyte environment during reaction,²⁸ much less its impacts on NO₃RR activity and selectivity. This gap in understanding is largely due to the micron-scale and dynamic nature of the interfacial electrolyte environment, which makes it inherently challenging to probe experimentally. 15,16,22 To this end, computational simulations using continuum models have shown promise as a high-fidelity, computationally efficient approach to describe interfacial electrolyte properties. ^{29–32}

Although their physicochemical properties differ, the interfacial and bulk electrolytes are bridged by mass transport phenomena. During electrochemical NO₃RR, the anionic reactant nitrate must travel against the electric field generated by the often negatively charged electrode and specifically adsorb to the electrode surface. A broad, multiphase portfolio of products can be generated at the electrode (e.g., hydroxide ions, nitrite, dinitrogen, ammonia), many of which can undergo homogeneous acid-base reactions and in turn influence the interfacial electrolyte environment.³³ Meanwhile, HER competes with NO₃RR and contributes to modifying the interfacial electrolyte environment. Because mass transport governs the supply of reactant and dissipation of products, it influences interfacial electrolyte properties that impact the activity of NO₃RR and concurrent HER as well as the selectivity of NO₃RR (altogether referred to here as NO₃RR performance). In both fundamental studies and large-scale applications, mass transport often limits NO₃RR activity^{9,34} and was found to impact NO₃RR selectivity. 35,36 However, current understanding of their underlying mechanisms remains insufficient for informing process engineering. More broadly, several characteristics of NO₃RR make it a suitable "model reaction" to study mass transport effects in electrocatalytic reduction reactions: (1) improved control of reactant speciation and concentration, compared to, e.g., CO_2RR $(CO_{2(g)}$ vs $CO_{2(aq)}$ vs $H_2CO_{3(aq)})$; $^{35-40}$ (2) enhanced opportunities to investigate reaction selectivity, compared to, e.g., HER; and (3) sufficient but not prohibitive complexities for computational simulations. Therefore, we purposely imposed (rather than minimized, as required in reaction kinetic studies) the mass transport limitation to elucidate mass transport effects in NO₃RR. We systematically controlled the extent of mass transport and investigated: (1) how mass transport influences NO₃RR performance, (2) how mass transport modulates the interfacial electrolyte environment, and (3) how properties of the interfacial electrolyte environment impact the reaction activity and selectivity.

Recognizing the pivotal role of the interfacial electrolyte environment, we approached the mass transport effects from a microscopic perspective by combining electrochemical experiments, continuum model simulations, and spectroscopic characterizations. We conducted electrochemical experiments in a representative and translational membrane-separated flow cell, using planar polycrystalline titanium (Ti) foil as a generic NO₃RR electrode. We imposed the mass transport limitation

with a sufficiently negative applied potential; by varying the electrolyte flow rate, we tuned the extent of mass transport and evaluated its influence on NO₃RR performance. A diffusionmigration-reaction model (generalized-modified Poisson-Nernst-Planck, GMPNP) was employed to simulate the interfacial electrolyte properties and illustrate their dependence on mass transport. Using experimental electrochemical data as model inputs, spatial profiles of electric potential and species concentration under the investigated flow conditions were resolved. Informed by this descriptive model, we further deconvoluted effects of interfacial pH and background electrolyte concentration by conducting flow cell experiments under varied bulk electrolyte properties and measuring in situ pH with the aid of attenuated total reflectance-surfaceenhanced infrared absorption spectroscopy (ATR-SEIRAS). We found that enhanced mass transport promotes NO₃RR activity by promoting the diffusion of nitrate but lowers ammonia selectivity by increasing the interfacial pH, exhibiting an activity-selectivity trade-off. Situated in NO₃RR, this study illustrates microscopic mechanisms of mass transport effects and also provides broadly applicable insights on the role of mass transport in defining the reaction microenvironment in energy-relevant electrocatalytic reduction reactions.

METHODS

Electrochemical Nitrate Reduction Experiments and Product Analysis. All electrochemical NO₃RR experiments were conducted in a custom airtight system consisting of a two-chamber membrane-separated flow cell and an electrolyte reservoir, unless otherwise specified. The electrolyte was recirculated between the electrochemical flow cell and the electrolyte reservoir; the electrolyte flow rate was controlled by peristaltic pumps (Figure S1 in the SI). A three-electrode configuration was always employed, consisting of a Ti working electrode (5.4 cm² geometric area), a platinum counter electrode, and a Ag/AgCl reference electrode; all potentials were converted to the reversible hydrogen electrode (RHE) scale using the initial measured bulk pH. A cation exchange membrane (Nafion) separated the working and counter electrode chambers. All electrochemical experiments were conducted using 85% IR compensation, and all current densities reported were based on geometric electrode area.

For each NO_3RR experiment, identical electrolytes were added to the working and counter electrode chambers. Before and after each experiment, electrolytes from both chambers were sampled for pH measurement and aqueous product analysis. Nitrate and nitrite concentrations were quantified using anion chromatography, and ammonia concentration was quantified using spectrophotometric flow injection analysis. Because homogeneous acid—base equilibria exist in the electrolyte, we reported the sum concentrations of conjugate acid—base pairs: nitrite refers to the sum of nitrite and nitrous acid, and ammonia refers to the sum of ammonia and ammonium. Gaseous products (H_2 and N_2) were analyzed by in-line gas chromatography. N_2 was not detected with a lower detection limit of 50 ppm (corresponding to 0.091 mA/cm² partial current density). Complementary experimental details are given in SI Section S1.1–1.2.

For each NO₃RR reaction condition (listed in Table S3), triplicate experiments were performed, and the average and standard deviation were shown for all reported values. For all liquid samples from each NO₃RR experiment, triplicate measurements were conducted, and the average was used in calculating performance metrics. Total and product partial current densities, time-averaged nitrate removal rate, Faradaic efficiency (FE), and nitrogen selectivity (N-selectivity) were used as key metrics to assess NO₃RR performance (definitions in SI Section S1.3). Control experiments were conducted to confirm negligible contamination and detection noise in ammonia production (SI Section S1.8).

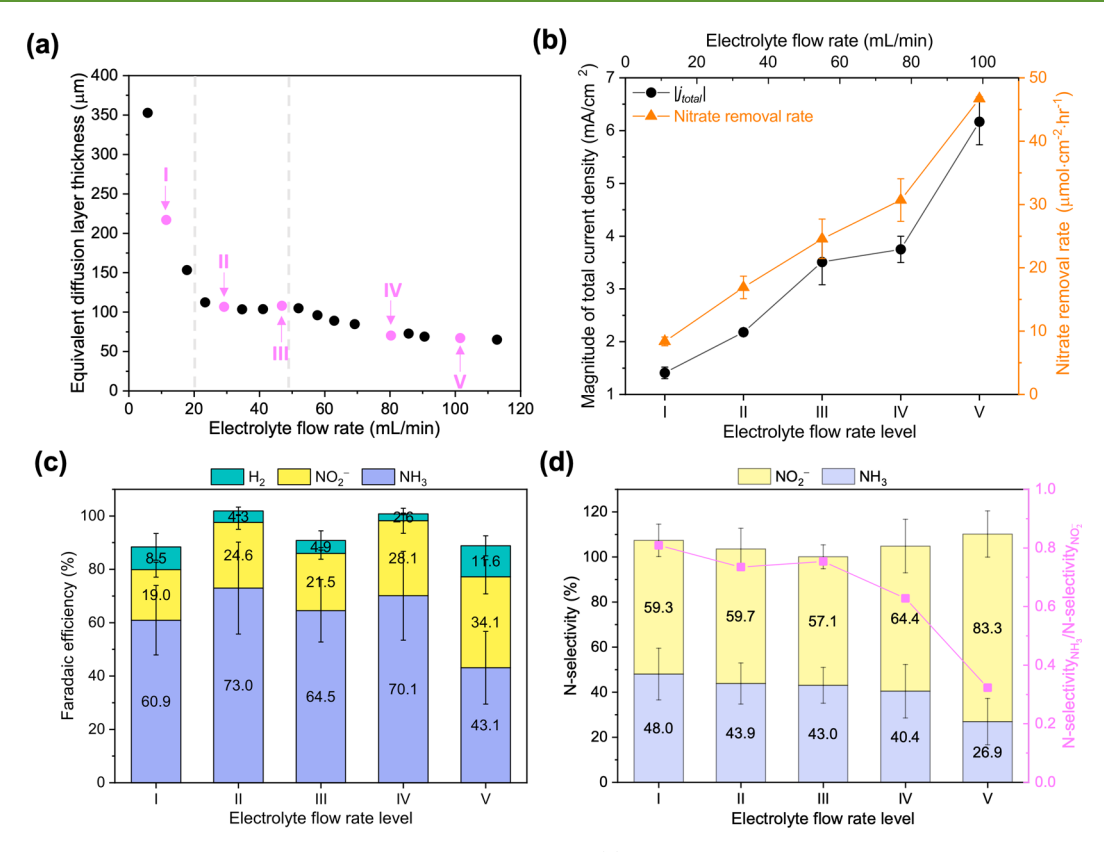


Figure 1. Experimental demonstration of mass transport effects in NO_3RR . (a) Empirically determined equivalent diffusion layer thickness as a function of electrolyte flow rate. Three distinct regimes are segmented by dashed lines. Flow rates applied in electrochemical NO_3RR experiments are highlighted in magenta. Detailed values are tabulated in Table S1. (b) Absolute values of total current density (left axis) and time-averaged nitrate removal rate (right axis), (c) Faradaic efficiency, and (d) N-selectivity (left axis) and ammonia to nitrite N-selectivity ratio (magenta squares, right axis) in the concentrated background (1 M $NaClO_4 + 10$ mM HNO_3) at designated electrolyte flow rate levels. Potentiostatic experiments were conducted at $-1.0 V_{RHE}$ for 90 recirculation events (experiment durations in Table S9). Error bars represent \pm one standard deviation. Error bars on N-selectivity ratios are given in Figure S15.

Continuum Model Summary. To simulate interfacial electrolyte properties under NO_3RR reaction conditions, we adapted the GMPNP originally developed for CO_2RR^{29} because of several advantages: (1) the continuum treatment of the electrolyte circumvents the prohibitively high computational cost of *ab initio* simulations for regions larger than the nanometer scale, (2) the inclusion of migration enables the reconstruction of the EDL and illustrates how different time scales govern bulk and interfacial phenomena, which the reaction—diffusion model fails to capture, and (3) the inclusion of solvated species sizes to the PNP model facilitates derivation of physically relevant concentration profiles (i.e., below the steric limit). $^{29-32}$

The physical regions simulated in the GMPNP model are depicted in Figure 2a. This model simulated the time-dependent, onedimensional electric potential and species concentration profiles outside of the outer Helmholtz plane (OHP). The reactive transport of species within the simulation zone was calculated via the generalized-modified Nernst-Planck equations, the potential was treated with the Poisson equation, and the two sets of equations were solved self-consistently using the continuity equation. Primary reactions and model parameters are summarized in SI Section S2.1, and the governing equations were non-dimensionalized to improve numerical stability and computational efficiency. We used Dirichlet boundary conditions for the potential to be an integer multiplier of the thermal voltage referenced to the potential of zero charge (PZC) of the electrode at the OHP as well as for species concentrations at the right-hand boundary at the diffusion layer edge. The DFTcalculated PZC of the most likely surface species under reaction conditions, TiH₂, was used (-0.9 V_{RHE}).⁴² To simulate interfacial electrolyte properties under varying mass transport conditions, the

corresponding equivalent diffusion layer thickness, $\delta_{\rm eqv}$, and product partial current densities from NO₃RR experiments were used as Neumann boundary conditions at the OHP (Figure S10 and Table S8). The use of experimental current densities as a boundary condition rather than a physics-based approach (such as Butler–Volmer kinetics or a microkinetic model) renders this model descriptive, and it is thus best suited for applications where the user wishes to interpret experimental trends or determine spatial concentration and potential profiles.

The simulation time was chosen to be sufficient to fully establish the EDL (i.e., charge density within the EDL converged, the potential profile was unchanging, and concentrations of all ionic solutes change within 0.01% between timesteps). Because of the right-hand Dirichlet boundary conditions, a true steady state is difficult to achieve, and we refer to this condition as "pseudo-steady state" (SI Section S2.3). As demonstrated by Bohra et al., the autoionization of water is out of equilibrium within the EDL (i.e., $[H^+] \cdot [OH^-] \neq K_W$, 1.01×10^{-14} at 25 °C),²⁹ likely due to the neglected ion-ion interactions beyond steric effects within the GMPNP equations and the pseudo-steadystate condition within our simulations. Therefore, we defined pHequivalent (eq \$28) to quantitatively describe the interfacial electrolyte environment, which converts the relative abundance of H⁺ and OH⁻ into a value equivalent to the classical pH value under the same condition. Limitations of the GMPNP models are also discussed in SI Section S2.4.

Local pH Measurement Using ATR-SEIRAS. We used attenuated total reflectance-surface-enhanced infrared absorption spectroscopy (ATR-SEIRAS) to measure the interfacial pH under NO₃RR conditions. Because Ti does not exhibit the surface enhancement effect, ⁴³ a thin layer of copper (Cu, <100 nm) was

deposited onto a germanium crystal for use as the working electrode in ATR-SEIRAS experiments in a custom single-chamber, three-electrode electrochemical cell. *In situ* pH measurements were performed in acidic and neutral phosphate buffer electrolytes during chronoamperometry experiments, and the local pH was determined using a ratio of peak areas from the phosphate species (calibration range pH 1–13.5). Details on the ATR-SEIRAS cathode fabrication, pH calibration, and *in situ* pH measurement are given in SI Section S1.9.

RESULTS AND DISCUSSION

How Does Mass Transport Influence the Activity of NO₃RR and HER and the Selectivity of NO₃RR? To systematically examine mass transport effects in NO₃RR, we first quantified the dependence of mass transport conditions on flow conditions. We used a flow cell to enable facile product quantification under varying mass transport conditions and to provide translational insights toward continuous-flow implementation. Flow cell results were related to rotating disk electrode (RDE) experiments using an equivalent diffusion layer thickness measured at a series of electrolyte flow rates (see SI Section S1.4). As expected, δ_{eqv} generally decreased with increasing flow rate (Figure 1a). Although all flow rates studied corresponded to laminar flow, three distinguishable $\delta_{\rm eqv}$ regimes were observed: a drastic decrease in $\delta_{\rm eqv}$ under low flow rates, a nearly constant δ_{eqv} under medium flow rates, and a gradually decreasing $\delta_{
m eqv}$ under high flow rates, approaching 65 μ m at the flow rate of 113 mL/min (maximum flow rate without causing electrolyte leakage). Notably, this highest accessible flow rate translates to an RDE rotation rate of below 50 RPM in a typical setup (15 mm disk outer diameter), highlighting that the flow cell facilitates investigation of mass transport conditions in the low-mixing region with higher resolution than RDE. Five electrolyte flow rates (flow rates I to V, from 11.5 to 101.5 mL/min, Table S1) spanning all three regimes were thus applied in NO₃RR experiments.

We isolated the effects of mass transport by keeping several parameters constant across our experiments, including the NO₃RR electrocatalyst, initial nitrate concentration, background electrolyte, and applied potential. Polycrystalline Ti was used as a generic NO₃RR electrocatalyst because of its appreciable $\rm NH_3$ selectivity, abundance, moderate cost, and corrosion resistance. ^{25,42} We used 10 mM nitrate to reflect our application goal of treating dilute nitrate-polluted feedstocks (e.g., municipal wastewater, agricultural runoff) as opposed to the commonly used higher nitrate concentrations in the NO₃RR literature (0.1-1.0 M; SI Section S1.5).^{4,9,44} The background electrolyte was fixed as NaClO₄ (with varied concentrations) to leverage a weakly adsorbing anion (ClO₄) that minimizes surface site blocking 45,46 and a common wastewater cation (Na⁺) with moderate ion size and acidity to represent cation effects.^{23,47} We performed potentiostatic experiments at a sufficiently negative value (-1.0 V_{RHE}, SI Section S1.7) where NO₃RR is not kinetically limited under the five designated flow rates. We first examined the flow rate dependence of NO₃RR performance (i.e., activity of NO₃RR and HER and selectivity of NO₃RR) in 1 M NaClO₄ + 10 mM HNO₃ electrolyte (referred to as the concentrated background). To prevent the possible influence of electrolyte flow rate on reaction progress, ^{48,49} a fixed recirculation event number was used across different flow rates (i.e., reaction duration inversely proportional to flow rate, Table S9).

NO₃RR activity, as captured by the time-averaged nitrate removal rate, generally increased with increasing flow rate

(Figure 1b). This activity trend confirmed that NO₃RR was subject to mass transport limitations under this applied potential across all five flow rates. Under a higher flow rate, a thinner diffusion layer posed less mass transport resistance, leading to a faster delivery of reactant to the electrode surface and a higher reaction rate. We further confirmed that NO₃RR activity was limited by the mass transport of nitrate (with experiments using an elevated nitrate concentration, SI Section S3.1.2). In contrast to the monotonic trend of NO₃RR activity with respect to flow rate, the activity of the competing HER (captured by the H₂ partial current density) did not show clear flow rate dependence (Figure S14). Combined with cyclic voltammetry features (Figure S5), this independence indicated that water reduction was the main HER mechanism under the applied potential (-1.0 V_{RHE}) because the concentration of reactant water was not affected by mass transport conditions. Additionally, despite operation at a very negative potential and a dilute nitrate concentration (10 mM), HER only comprised at most 14% FE (Figure 1c). Because NO₂RR dominated, the total current density followed the same monotonic trend with flow rate as the nitrate removal rate.

For NO₃RR selectivity, two observations were shared across all flow rates (Figure 1d). First, nitrite and ammonia accounted for almost all NO₃RR products (combined N-selectivity approximately 100%). Second, nitrite was the majority nitrogen product (i.e., N-selectivity_{NO}, > 50%). However, the distribution between the two nitrogen products (Nselectivity_{NH₃}/N-selectivity_{NO₂}, magenta symbols in Figure 1d) changed slightly with flow rate, with NO₃RR favoring ammonia more under the lowest flow rate than under the highest flow rate. Because nitrite is a reaction intermediate in the reduction of nitrate to ammonia, we conducted longduration experiments (250 min, SI Section S3.1.3) and confirmed that the observed N-selectivity trend held and was independent of the reaction time (Figure S18). Taken together, the flow rate dependence of NO₃RR selectivity implied that the interfacial electrolyte environment was modified by mass transport and influenced further reduction from nitrite to ammonia. Experiments were repeated under all five flow rates for a fixed reaction duration of 30 min, and similar activity and selectivity trends were established (SI Section S3.1.4). We therefore kept the reaction time as 30 min in subsequent potentiostatic experiments.

How Does Mass Transport Modulate the Interfacial Electrolyte Environment? Elucidating experimentally observed effects of mass transport on NO₃RR performance requires a microscopic perspective of the interfacial electrolyte environment. We adapted the GMPNP model, which has successfully described CO₂RR in non-dilute electrolyte (>10 mM),²⁹ to characterize the interfacial electrolyte environment outside of the OHP under NO₃RR conditions. The empirically determined diffusion layer thickness and product partial current densities from potentiostatic NO₃RR experiments in the concentrated background (Figure 1) were used as model inputs. GMPNP simulations output the spatial distribution of electric potential, background electrolyte solutes, NO₃RR reactants and products, and pH-equivalent at the pseudosteady state under the flow rates studied (model details in Methods).

Moving from the OHP to the bulk, the simulated electric potential logarithmically extinguishes to zero within approximately 2 nm (Figure S21a,b), which corresponds to the diffuse

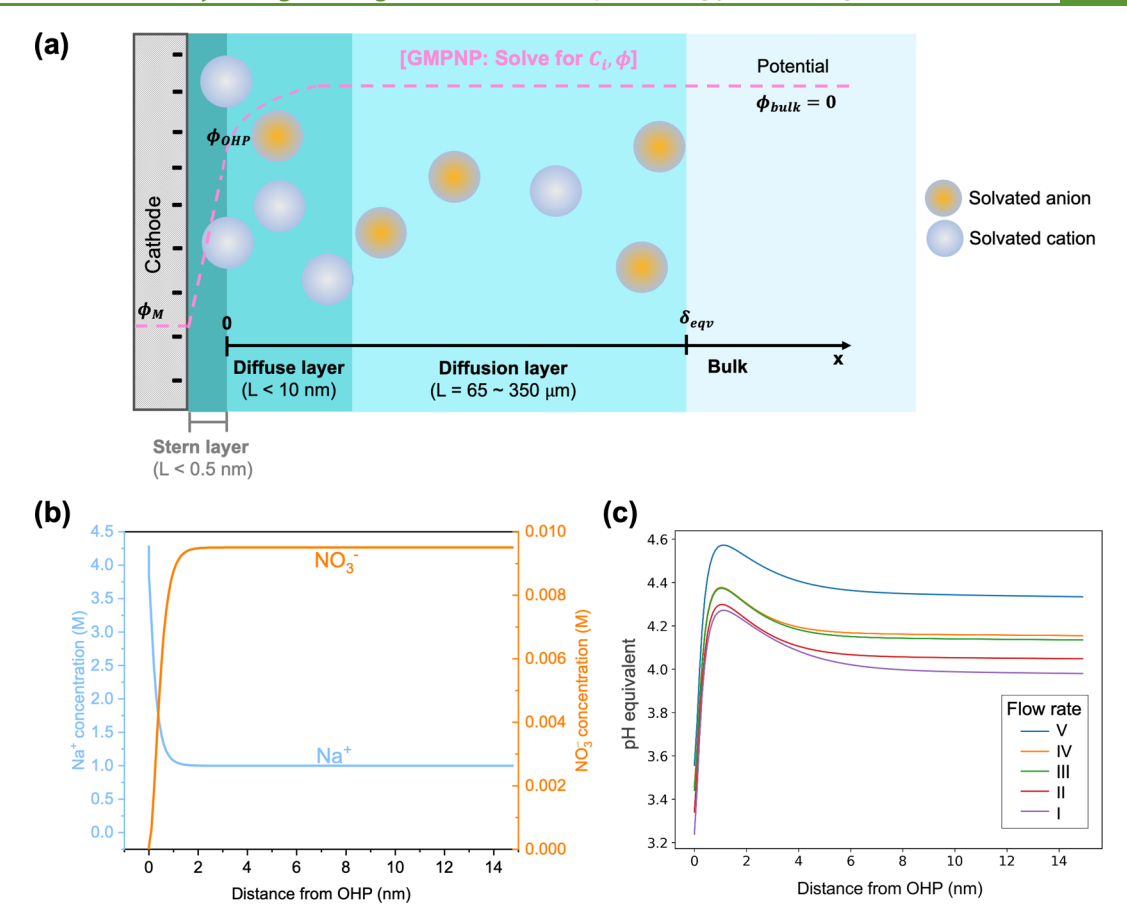


Figure 2. Computational simulation of interfacial electrolyte properties under different flow rates. (a) Schematic of the different mass transport regions simulated in the GMPNP model. The EDL consists of a Stern layer (also known as the Helmholtz layer, contains specifically adsorbed species) and the diffuse layer. The origin of the x-axis is located at the OHP. GMPNP simulated (b) profiles of Na $^+$ concentration (left axis) and nitrate concentration (right axis) under flow rate V, and (c) profiles of pH-equivalent under flow rate I–V in the diffuse layer. All simulations were conducted in 1 M NaClO $_4$ + 10 mM HNO $_3$ at -1.0 V $_{\rm RHE}$, using electrochemical results from potentiostatic experiments with a fixed recirculation event number as inputs (Figure 1). Complementary simulation results plotted at different distance scales and for other interfacial electrolyte properties are shown in SI Section S3.1.5.

layer. Within the same region, the background cation (Na⁺) concentration decays from 4.3 M (the steric limit) to its bulk value of 1 M (Figure 2b). The aggregation of cations at the OHP is due to their electrostatic attraction to the cathode and has been observed both computationally 13,50,51 and experimentally.⁵² The resultant high local cation concentration can substantially impact reaction activity and selectivity by interacting with reaction intermediates or modifying the interfacial electric field and pH; 13,23,24,27,53 however, their putative molecular mechanisms cannot be explicitly simulated using the GMPNP model alone. Nevertheless, the fact that Na⁺ concentration profiles do not differ appreciably across all flow rates (Figure S21c,d) suggests that the aggregation of Na⁺ influences NO₃RR similarly across mass transport conditions. Converse to Na⁺, the background anion (ClO₄⁻) concentration is lower in the EDL than in the bulk due to electrostatic repulsion and does not change with flow rate (Figure S22a,b). With much higher bulk concentrations than other ionic solutes, Na⁺ and ClO₄⁻ are the major constituents of the EDL. From the bulk to the OHP, the nitrate concentration first declines gradually in the diffusion layer and then drops sharply by an order of magnitude within the EDL (Figure 2b, Figure S22c), due to its consumption during NO₃RR and electrostatic repulsion with the cathode (similar to ClO₄). Although the GMPNP model does not describe the region within the OHP,

the near-complete depletion of nitrate in the diffuse layer rationalizes the observation that NO₃RR is subject to mass transport limitations for nitrate.

The experimentally observed basification phenomenon is also reproduced in GMPNP simulations. The pH-equivalent profile exhibits a non-monotonic trend traversing simulated regions (Figure 2c): within the diffuse layer, the pH-equivalent is the lowest at the OHP, suggesting that the electrostatic repulsion of OH outweighs its production in both heterogeneous and homogeneous reactions; beyond the relative maximum at ca. 2 nm outside the OHP, the pHequivalent decreases to its bulk value in the diffusion layer (Figure S22e). Under higher flow rates, the pH-equivalent profile is uniformly higher across all simulated regions. Although simulated pH-equivalent values do not equal actual pH values under input reaction conditions due to the pseudosteady-state assumption, a clear trend is established: a higher flow rate generates a more alkaline local environment, suggesting that the intensified production of OH⁻ outpaces its intensified dissipation. Because the trends for pH-equivalent and N-selectivity_{NH3}/N-selectivity_{NO2} coincide, we hypothesized that the interfacial pH mediates the distribution between the two nitrogen products.

In addition to OH⁻, many nitrogen products from NO₃RR, including NH₄⁺ and NO₂⁻, can also modify the interfacial

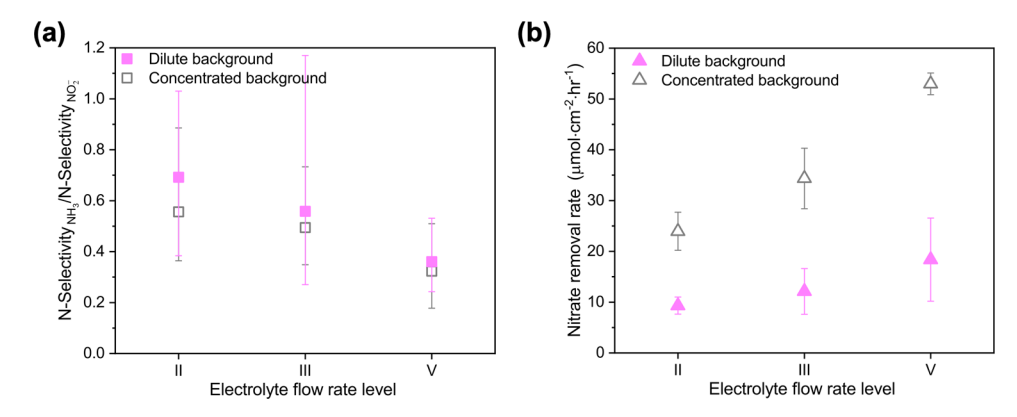


Figure 3. Background electrolyte concentration effects. Comparison of 30 min potentiostatic experiment ($-1.0~V_{RHE}$) results in dilute (magenta, filled) and concentrated backgrounds (gray, unfilled), (a) ammonia to nitrite N-selectivity ratio, and (b) time-averaged nitrate removal rate at designated electrolyte flow rate levels. Dilute background: 10 mM NaClO₄ + 10 mM HNO₃, concentrated background: 1 M NaClO₄ + 10 mM HNO₃. Asymmetric error bars in panel (a) come from propagating errors in ammonia and nitrite N-selectivity; error bars in panel (b) represent \pm one standard deviation.

electrolyte environment by buffering the pH and constituting the EDL. However, on the timescale of our GMPNP simulations, we found that such modifications introduced by nitrogen products are likely to be insignificant. First, the diffusive driving force shortens the residence time of NH₄ and NO₂ in the EDL before they are transported into the diffusion layer, and their homogeneous acid-base equilibria during the short stay are outpaced by the production of OH⁻ in NO₃RR, leading to little buffering effect in the EDL region. Second, concentrations of NH₄ and NO₂ and their conjugate acidbase pairs are orders of magnitude lower than those of the background ions, contributing negligibly to the EDL structure (Figures S23 and S24). The NH₃/NH₄ equilibria result in both NH₄ and NH₃ concentrations being $O(10^{-4})$ M and $O(10^{-5})$ M, respectively, whereas NO_2^- is nearly depleted $(C_{NO_{3}} \sim O(10^{-6}) \text{ M})$ because the equilibrium heavily favors HNO_2 formation ($C_{HNO_2} \sim O(10^{-4})$ M). Across different flow rates, nitrogen product concentration profiles exhibit the same trend as their corresponding partial current densities. Essentially, we viewed the simulated nitrogen product profiles as the consequence, rather than the cause, of the experimentally observed NO₃RR performance.

To summarize, GMPNP simulations reproduced the interfacial electrolyte environment that exhibits a layered structure. With increasing electrolyte flow rate, the diffusion layer shrinks, enhancing the nitrate diffusion driving force and consequently the NO₃RR activity. However, the compact EDL structure (size and composition) remains almost unperturbed, in line with the experimental observation that the NO₃RR product portfolio was largely unaltered by the flow rate. Meanwhile, the interfacial environment becomes more alkaline due to the higher total current density, hypothetically shifting the NO₃RR selectivity toward nitrite.

How Do Interfacial Electrolyte Properties Influence NO_3RR Performance? Although GMPNP simulations add microscopic insights to the reaction microenvironment during NO_3RR , they provide only hypotheses regarding the selectivity trend. On one hand, the flow rate dependence of pH-equivalent agreed with that of N – selectivity_{NO_2}, indicating that interfacial pH mediates the nitrogen product selectivity. On the other hand, despite being unaltered by the flow rate, the extremely high interfacial Na^+

concentration can also profoundly impact reaction mechanisms. 13,23,24,27,53 Therefore, to examine hypotheses on the origin of mass transport effects on $\mathrm{NO_3RR}$ selectivity, we sought to elucidate specific influences of interfacial pH and $\mathrm{Na^+}$ concentration. We intentionally tuned bulk electrolyte compositions to vary the interfacial electrolyte properties and compared $\mathrm{NO_3RR}$ performance under the same mass transport conditions. GMPNP simulations, ATR–SEIRAS measurements, and pulsed potential experiments were leveraged to explicitly identify contributions from different interfacial properties.

Background Electrolyte Concentration Governs the NO₃RR Activity. To investigate the influence of interfacial cation concentration on NO₃RR performance without introducing another cationic species, we varied the background electrolyte concentration. With dilute feedstocks as our treatment targets, we investigated the scenario where the background electrolyte concentration was equimolar with the reactant nitrate (10 mM NaClO₄ + 10 mM HNO₃, referred to as the dilute background) at the same potential $(-1.0 \text{ V}_{\text{RHE}})$ and under flow rates II, III, and V; complementary GMPNP simulations were performed to characterize the new interfacial electrolyte environment. Simulations revealed a similar accumulation of Na+ at the OHP, but the steric limit is not reached and the interfacial Na+ concentration is about 9 times lower than in the concentrated background (ca. 0.49 M, Figure S25c). Furthermore, the dilute background dramatically changes the EDL structure. The EDL becomes more disperse, with the diffuse layer extending to ca. 10 nm from the OHP due to the lower total concentration of all ionic solutes. Due to equimolar HNO3 and background electrolyte, NO3 and H+ become more significant EDL constituents (Figure S29). However, the interfacial pH-equivalent remains on the same order of magnitude and shows a similar flow rate dependence with that in the concentrated background (Figure S27, higher local pH at higher flow rate).

Despite this 9-times lower interfacial $\mathrm{Na^+}$ concentration, experimentally measured $\mathrm{NO_3RR}$ selectivity was not significantly affected by the background electrolyte concentration. In the dilute background, nitrite remained the predominant nitrogen product across all flow rates (Figure S32d) with similar $\mathrm{N-selectivity_{NH_3}/N-selectivity_{NO_2^-}}$ to concentrated background experiments under the same flow rate (Figure

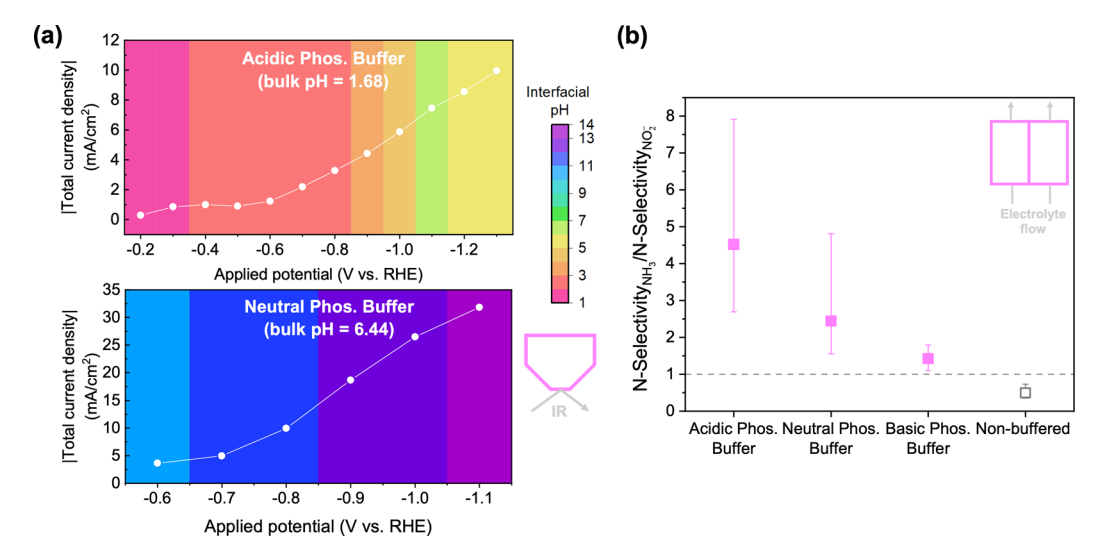


Figure 4. Interfacial pH effects. (a) Absolute values of total current density (y axis) and measured interfacial pH (color mapped background) as functions of applied potential in ATR–SEIRAS experiments on Cu electrodes, in acidic and neutral phosphate buffers. (b) Comparison of ammonia to nitrite N-selectivity ratios from 30 min potentiostatic ($-1.0 \, V_{RHE}$) flow-cell experiments in phosphate buffer (filled) and non-buffered (unfilled) electrolytes. Insets: conceptual diagrams of corresponding cell configurations. Compositions of all electrolytes are given in Table S3. Error bars represent \pm one standard deviation.

3a). Given the substantial impacts that cations could introduce to reaction energetics (by modifying the electric field or interacting with reaction intermediates), ^{23,24,47} this insensitivity of nitrogen product distribution to the interfacial Na⁺ concentration implied that on Ti, the further reduction of nitrite to various nitrogen products (including ammonia) is not controlled by intermediate adsorption energy. ^{3,6} The experimentally observed insensitivity of nitrogen product distribution also suggested that potential pH-modifying effects from cations (e.g., hydrolysis of their solvation shells²³) are not significant enough to shift NO₃RR selectivity under mass transport limitations.

Although the hypothesized cation effects on NO₃RR selectivity were not observed, the NO₃RR activity differed drastically between the dilute and concentrated background experiments. Under the same flow rate, both the time-averaged nitrate removal rate (Figure 3b) and total current density (Figure S32a) in the dilute background were about half of the values in the concentrated background. This greatly lowered NO₃RR activity could not be completely explained by the loss of applied potential to the higher uncompensated solution resistance in the dilute background (i.e., Ohmic drop, SI Section S3.2.2). The activity difference was also not introduced by enhanced competition from HER (Figure S32b), as was found in some $\rm CO_2RR$ cases. 31,54 Instead, combined adverse effects from a higher nitrate mass transport resistance (Figure S30) and a lower interfacial Na⁺ concentration were likely accountable. Because the rate determining step (RDS) in NO₃RR on most metals is the adsorption of nitrate and its ensuing reduction into nitrite, 2,3,5,6 and cations can facilitate the RDS by forming ion pairs with nitrate²⁷ or stabilizing intermediate states, 23,24,51 the significantly lower interfacial Na⁺ concentration could lower the NO₃RR activity.

For dependence on the electrolyte flow rate, the dilute background shared similar trends with the concentrated background for both NO₃RR activity and selectivity. Overall, these results suggested that while the background electrolyte concentration directly influences the EDL structure and governs NO₃RR activity, interfacial cation concentration is

not the principal factor in determining NO_3RR selectivity. Thus, we speculated that the interfacial pH steers NO_3RR selectivity.

Interfacial pH Steers the NO₃RR Selectivity. To experimentally investigate how the interfacial pH influences NO₃RR, we attempted to maintain the interfacial pH close to the bulk pH by adding phosphate buffer and varied the bulk pH by varying phosphate buffer compositions. We used three 0.5 M phosphate buffers with pH 1.7, 6.5, and 10.5 as electrolytes (referred to as acidic, neutral, and basic phosphate buffers, respectively), while keeping nitrate concentration constant (10 mM) and Na+ concentration as close to the concentrated background electrolyte as possible (compositions in Table S3). Potentiostatic experiments were conducted at the same applied potential $(-1.0 V_{RHE})$ and under the intermediate flow rate III. Although the increase in the bulk pH after 30 min experiments was at most 1.3 units in all three buffers (Figure S33a), in situ pH measurements demonstrated limited buffering effects of phosphate species on the interfacial pH.

We leveraged the surface-sensitive feature of ATR-SEIRAS to measure in situ pH via phosphate speciation at the electrode-electrolyte interface under reaction conditions. By determining the ratio of phosphate species, ATR-SEIRAS probed the average pH in the first 5 to 10 nm of stagnant electrolyte 43,55,56 from a Cu electrode under NO₃RR conditions (see Methods). Despite differences in cell configuration and NO₃RR performance on Cu and Ti,³⁰ ATR-SEIRAS experiments provide relatable insights that explain our experimental results on Ti. Under applied potentials more negative than $-0.6~V_{RHE}$, the interfacial pH was much higher than the bulk pH (Figure 4a); furthermore, the surge in the interfacial pH was nearly instantaneous upon the application of potential (Figure S34). The local alkalinization was drastic enough that the interfacial pH exceeded 12 under $-1.0~V_{RHE}$ in the neutral buffer, aligning with previous observations. Nonetheless, the measured interfacial pH was consistently lower in the acidic buffer than in the neutral buffer under the same applied potential. These in situ pH measurements revealed that, among flow-cell

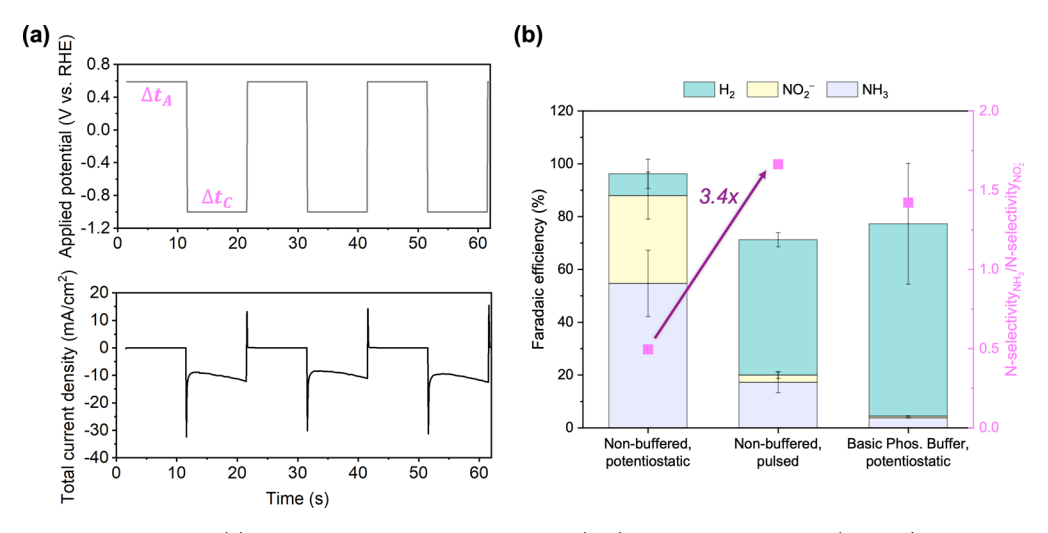


Figure 5. Pulsed potential experiments. (a) Pattern of applied pulsed potential (top) and current response (bottom). Pulsed potential experiments were conducted in 1 M NaClO₄ + 10 mM HNO₃, with $E_C = -1.0$ V_{RHE}, $\Delta t_C = 10$ s, $E_A = +0.6$ V_{RHE}, $\Delta t_A = 10$ s, and total experiment time of 60 min. (b) Comparison of Faradaic efficiency (left axis) and ammonia to nitrite N-selectivity ratio (magenta squares, right axis) from pulsed potential and potentiostatic experiments under flow rate III. Compositions of all electrolytes are given in Table S3. Error bars in panel (b) represent \pm one standard deviation. Error bars on N-selectivity ratios are given in Figure S37.

experiments, the interfacial pH was uniformly higher than the bulk pH and expected to follow the trend of acidic buffer < neutral buffer < basic buffer during NO₃RR. Notably, the final bulk pH in the non-buffered concentrated background experiment (30 min, flow rate III) exceeded that in the basic buffer experiment. Thus, the interfacial pH in the non-buffered experiment was likely the highest, surpassing the basic buffer for the majority of the NO₃RR duration.

Building on this trend, we analyzed effects of the interfacial pH on NO₃RR performance across flow-cell experiments in phosphate buffers and the non-buffered concentrated background. Strikingly, we found that HER outcompeted NO₃RR to be the major electrode reaction in all three phosphate buffers (FE_{H₂} > 50%, Figure S33c), with the H_2 partial current density being two orders of magnitude higher than in the nonbuffered electrolyte. This substantial enhancement of HER could result from two factors: (1) phosphate species act as buffers that lower the interfacial pH, which increases the surface coverage of $H_{(ads)}$ and the thermodynamic favorability of H₂ formation 42 and (2) phosphate species act as exogenous proton donors and contribute to HER through electrochemical deprotonation.^{57–59} Despite the likelihood of these qualitative explanations, we refrained from directly connecting HER activity with the interfacial pH. Because the identity and concentration of viable proton donors (e.g., H₃O⁺, H₂O, H₃PO₄, H₂PO₄, HPO₄²⁻) varied with the interfacial pH, it was not possible to identify the dominant HER mechanisms nor to further deconvolute contributions from the interfacial pH and proton donor speciation on HER activity. The nitrate removal rate was on the same order of magnitude across all three phosphate buffers and the non-buffered electrolytes (Figure S33b), insensitive to both the interfacial pH and proton donor speciation. It could originate from two primary factors: (1) NO₃RR activity was controlled by mass transport conditions, which was kept constant across the four electrolytes compared, as confirmed by the monotonically increasing trend with flow rate in the acidic buffer (Figure S35b), and (2) it is likely that the elementary step(s) that does not involve protons (e.g., nitrate adsorption, deoxygenation) controls the

RDS of NO_3RR on Ti, 3,6,10,42 making its activity intrinsically less sensitive to the abundance or identity of proton donors compared to reactions where the RDS is controlled by proton-transfer (PT) or concerted proton-electron-transfer (CPET) steps. 57

In contrast, NO₃RR selectivity varied profoundly across the compared electrolytes. Among the phosphate buffer experiments, the ammonia partial current density increased by about 2.5 times from basic to acidic buffers (Figure S33d, whereas the nitrite partial current density was not appreciably different). The observation of acidic conditions favoring ammonia production is consistent with studies on Ti and Cu, 25,26 although our observations of interfacial pH add nuance to previous observations based solely on bulk pH. Additionally, a reaction pathway besides ammonia was facilitated in the basic buffer, signaled by an undetermined nitrogen product(s) comprising 60% of total N-selectivity (Figure S33e). As for the nitrite to ammonia pathway, ammonia was substantially favored in all buffered electrolytes (Figure 4b), with N-selectivity_{NH},/N-selectivity_{NO} following the trend: acidic buffer > neutral buffer > basic buffer > 1 (i.e., equimolar ammonia and nitrite produced) > non-buffered. Moving from acidic to basic buffers, as the interfacial pH increased, the N-selectivity ratio gradually approached that in the non-buffered system, which exhibited the highest interfacial pH. Similar trends between the interfacial pH and N $selectivity_{NH_3}/N-selectivity_{NO_2}$ once again demonstrated that the interfacial pH is crucial to nitrogen product selectivity. However, like the complication in interpreting HER activity, because the identity and concentration of viable proton donors differed in phosphate buffers, the proton donor speciation effects on NO₃RR selectivity cannot be excluded.

Distinguishing the contribution of interfacial pH on selectivity requires techniques that regulate pH without introducing exogeneous proton donors. Therefore, we applied pulsed potential to periodically replenish the EDL, alleviate the accumulation of OH⁻,^{22,38,60} and create a less alkaline interfacial pH environment during NO₃RR. Pulsed potential experiments were conducted in the non-buffered, concentrated

background electrolyte under flow rate III. The same cathodic potential (E_C) of -1.0 V_{RHE} was used, and the anodic potential $(E_{\rm A})$ was chosen as +0.6 $V_{\rm RHE}$, slightly below the open circuit potential Symmetric pulse lengths were applied ($\Delta t_c = \Delta t_A = 10$ s, Figure 5a) that are long enough to fully establish the EDL under NO₃RR conditions (SI Section S2.3), and the effective reduction reaction time was kept at 30 min. Drastically different FE and nitrogen product distribution from potentiostatic experiments were generated in pulsed potential experiments (Figure 5b): HER was substantially enhanced, with FE_{H2} exceeding 50%; ammonia replaced nitrite as the dominant nitrogen product, and a 3.4-fold N-selectivity_{NH},/Nselectivity_{NO}- ratio was achieved. Without complications from proton donor speciation, this dramatic change in selectivity of NO₃RR vs HER and of ammonia vs nitrite and the great resemblance to the basic phosphate buffer provided strong evidence that a lower interfacial pH (rather than phosphate species acting as proton donors) primarily accounted for promoting HER and ammonia production in phosphate buffers.

Combining the flow rate dependence of experimentally measured N-selectivity ratios with pH-equivalent simulated by GMPNP and with in situ pH determined by ATR-SEIRAS, we concluded that the interfacial pH is the most likely mediator of mass transport effects on NO₃RR selectivity: a higher flow rate led to a higher interfacial pH, favoring nitrite production over ammonia. The following two mechanisms could help explain how interfacial pH influences NO₃RR selectivity. First, because the applied potential was calculated using the initial bulk pH and kept the same throughout potentiostatic experiments, a higher interfacial pH led to a lower effective potential during experiments, shifting the selectivity toward nitrite. 11,42,6 Second, it is still under debate whether the further reduction of nitrite to ammonia occurs through combination with preadsorbed H_(ads) or through direct interaction with proton donors (hydronium ions or water in the absence of buffers).^{3,10,26,28,35,62} Regardless, a lower interfacial pH corresponds to a higher $H_{(ads)}$ coverage on the electrode surface and/or a higher proton donor concentration near the electrode, promoting the sequential protonation steps beyond nitrite to produce ammonia. Furthermore, we propose that the N-selectivity_{NH₃}/N-selectivity_{NO₂} ratio acquired from postexperiment bulk phase analysis can be used as a readily accessible indicator of the interfacial pH. While the bulk pH after experiments under different flow rates differed significantly, the corresponding N-selectivity_{NO}ratios fell into the same regime (<1), suggesting that the interfacial pH during NO₃RR was similarly very alkaline for most of the reaction duration. This conclusion aligns with the earlier mentioned observation that water reduction was the main HER mechanism under all flow rates. Similarly, the interfacial pH in the dilute background is likely comparable with that in the concentrated background, whereas pulsed potential likely exhibits an interfacial pH similar to the basic phosphate buffer and much lower than the non-buffered potentiostatic experiments. We note that desorption of the reaction intermediate nitrite could also contribute to the Nselectivity change with flow rate, as it has been noted on other electrodes that dimensionless nitrite reduction rate constants and mass transfer coefficients are comparable.³⁵ Although nitrite adsorbs favorably on Ti, 42 it is possible that a higher

flow rate promotes the nitrite desorption and thus hinders its subsequent reduction to ammonia, by providing a higher diffusion (away) driving force for nitrite or deprotonating the nitric acid produced to form the anionic nitrite that desorbs more easily from the electrode surface. Overall, these results underscore that the interfacial electrolyte environment differs drastically from the bulk environment and can be engineered to optimize ammonia production.

CONCLUSIONS

In summary, we investigated how mass transport influences NO₃RR performance and elucidated the underlying mechanisms on Ti. By varying the electrolyte flow rate, we systematically controlled the mass transport extent in a flow cell and demonstrated its influence on activity of NO₃RR and HER as well as selectivity of NO₃RR. With continuum model simulations and ATR-SEIRAS, we characterized the interfacial electrolyte properties and deconvoluted their impacts on experimentally observed mass transport effects. We concluded that the diffusion layer thickness and the interfacial cation concentration govern the NO₃RR activity, whereas the interfacial pH steers the NO₃RR selectivity. Informed by these fundamental insights, we proposed engineering strategies to harness mass transport. NO₃RR activity can be enhanced by increasing the mass transport extent and the background electrolyte concentration; ammonia selectivity can be improved by preserving a low interfacial pH, but at the cost of decreased nitrate removal rate or intensified competition from HER. In addition, we demonstrated that pulsed potential is a powerful technique to tune the interfacial pH without changing the bulk electrolyte composition, which could help interrogate NO₃RR mechanisms and optimize ammonia production.

Although the interfacial cation concentration (0.5-4.3 M Na⁺ in this study) was not found to directly influence NO₃RR selectivity, we recognize that cation identity could be impactful, as has been demonstrated in CO₂RR. ^{13,24,31,52} We also emphasize the need for improved understanding of the identity and role of proton donors in NO3RR. In future studies, molecular-scale operando spectroscopic techniques (e.g., Fourier-transform infrared spectroscopy, Raman spectroscopy, laser scanning confocal microscopy) and multiscale computational methods^{63,64} (e.g., GMPNP interfaced with *ab* initio simulations) could enable a molecular view of the dynamic reaction microenvironment in NO3RR and its influence on reaction energetics. More broadly, this work provides a framework of combined electrochemical experiments, continuum model simulation, and in situ infrared spectroscopy to study the interfacial electrolyte environment in the ubiquitous but understudied mass transport-limited regime. Building on mechanistic understanding of mass transport effects in the convenient and representative model reaction of NO₃RR, this study will not only enable rational design of the reaction microenvironment to facilitate sustainable distributed ammonia manufacturing from wastewater but also provide unique insights on other important energy-relevant electrocatalytic reduction reactions. We believe that understanding and engineering the microscale reaction environment present enormous opportunities to help rebalance global biogeochemical cycles for nitrogen, carbon, and beyond.

ASSOCIATED CONTENT

Data Availability Statement

GMPNP model codes (freely available online: https://tinyurl.com/2fehd6rv).

Supporting Information

The Supporting Information is available free of charge at https://pubs.acs.org/doi/10.1021/acssuschemeng.3c01057.

Experimental details; supporting tables; simulation model details; and additional experimental and simulation data (PDF)

AUTHOR INFORMATION

Corresponding Author

William A. Tarpeh – Department of Chemical Engineering, Stanford University, Stanford, California 94305, United States; orcid.org/0000-0002-2950-526X; Phone: 650-497-1324; Email: wtarpeh@stanford.edu

Authors

Jinyu Guo — Department of Chemical Engineering, Stanford University, Stanford, California 94305, United States;
ocid.org/0000-0002-8775-3085

Paige Brimley — Department of Chemical and Biological Engineering, University of Colorado Boulder, Boulder, Colorado 80303, United States; Renewable and Sustainable Energy Institute, University of Colorado Boulder, Boulder, Colorado 80303, United States; orcid.org/0000-0002-9064-922X

Matthew J. Liu — Department of Chemical Engineering, Stanford University, Stanford, California 94305, United States; ⊕ orcid.org/0000-0002-8496-8267

Elizabeth R. Corson — Department of Chemical Engineering, Stanford University, Stanford, California 94305, United States; © orcid.org/0000-0003-2722-674X

Carolina Muñoz – Department of Chemical Engineering, Stanford University, Stanford, California 94305, United States

Wilson A. Smith – Department of Chemical and Biological Engineering, University of Colorado Boulder, Boulder, Colorado 80303, United States; Renewable and Sustainable Energy Institute, University of Colorado Boulder, Boulder, Colorado 80303, United States; orcid.org/0000-0001-7757-5281

Complete contact information is available at: https://pubs.acs.org/10.1021/acssuschemeng.3c01057

Notes

The authors declare no competing financial interest.

ACKNOWLEDGMENTS

We are grateful to several funders of this work, including the National Science Foundation EFRI program (Award 2132007) and the Chemical Engineering Department at Stanford University. J.G. and E.R.C. acknowledge support from the TomKat Center for Sustainable Energy. P.B. acknowledges support from the U.S. Department of Education Graduate Assistance in Areas of National Need Fellowship. M.J.L. acknowledges support from the National Aeronautics and Space Administration (NASA) Space Technology Graduate Research Opportunities fellowship (Award 80NSSC20K1207). Part of this work was performed at the Stanford Nano Shared Facilities (SNSF), supported by the National Science

Foundation under award ECCS-2026822. This work utilized the Summit supercomputer, which is supported by the National Science Foundation (Awards ACI-1532235 and ACI-1532236), the University of Colorado Boulder, and Colorado State University. The authors thank Dean M. Miller for support on the RDE setup, wastewater composition table, and inspiring discussions; Xi Chen for support on prototyping the reactor design; Joakim H. Stenlid and Michael T. Tang for insights on reaction mechanisms from the DFT perspective; Ankur Gupta and Charles B. Musgrave for enlightening discussions and feedback throughout the period of this work; and the Tarpeh group for critical feedback on the project.

REFERENCES

- (1) Abascal, E.; Gómez-Coma, L.; Ortiz, I.; Ortiz, A. Global Diagnosis of Nitrate Pollution in Groundwater and Review of Removal Technologies. *Sci. Total Environ.* **2022**, *810*, 152233.
- (2) Garcia-Segura, S.; Lanzarini-Lopes, M.; Hristovski, K.; Westerhoff, P. Electrocatalytic Reduction of Nitrate: Fundamentals to Full-Scale Water Treatment Applications. *Appl. Catal., B* **2018**, 236, 546–568.
- (3) Wang, Z.; Richards, D.; Singh, N. Recent Discoveries in the Reaction Mechanism of Heterogeneous Electrocatalytic Nitrate Reduction. *Catal. Sci. Technol.* **2021**, *11*, 705–725.
- (4) van Langevelde, P. H.; Katsounaros, I.; Koper, M. T. M. Electrocatalytic Nitrate Reduction for Sustainable Ammonia Production. *Joule* **2021**, *5*, 290–294.
- (5) Zeng, Y.; Priest, C.; Wang, G.; Wu, G. Restoring the Nitrogen Cycle by Electrochemical Reduction of Nitrate: Progress and Prospects. *Small Methods* **2020**, *4*, 2000672.
- (6) Wang, Y.; Wang, C.; Li, M.; Yu, Y.; Zhang, B. Nitrate Electroreduction: Mechanism Insight, in Situ Characterization, Performance Evaluation, and Challenges. *Chem. Soc. Rev.* **2021**, *50*, 6720–6733.
- (7) Galloway, J. N.; Townsend, A. R.; Erisman, J. W.; Bekunda, M.; Cai, Z.; Freney, J. R.; Martinelli, L. A.; Seitzinger, S. P.; Sutton, M. A. Transformation of the Nitrogen Cycle: Recent Trends, Questions, and Potential Solutions. *Science* **2008**, *320*, 889–892.
- (8) Tarpeh, W. A.; Chen, X. Making Wastewater Obsolete: Selective Separations to Enable Circular Water Treatment. *Environmental Science and Ecotechnology* **2021**, *5*, 100078.
- (9) Singh, N.; Goldsmith, B. R. Role of Electrocatalysis in the Remediation of Water Pollutants. ACS Catal. 2020, 10, 3365–3371.
- (10) Anastasiadou, D.; van Beek, Y.; Hensen, E. J. M.; Costa Figueiredo, M. Ammonia Electrocatalytic Synthesis from Nitrate. *Electrochem. Sci. Adv.* **2022**, No. e2100220.
- (11) Yu, S.; Louisia, S.; Yang, P. The Interactive Dynamics of Nanocatalyst Structure and Microenvironment during Electrochemical CO2 Conversion. *JACS Au* **2022**, *2*, 562–572.
- (12) Banerjee, S.; Gerke, C. S.; Thoi, V. S. Guiding CO2RR Selectivity by Compositional Tuning in the Electrochemical Double Layer. *Acc. Chem. Res.* **2022**, *55*, 504–515.
- (13) Ringe, S.; Clark, E. L.; Resasco, J.; Walton, A.; Seger, B.; Bell, A. T.; Chan, K. Understanding Cation Effects in Electrochemical CO2 Reduction. *Energy Environ. Sci.* **2019**, *12*, 3001–3014.
- (14) Fan, Q.; Bao, G.; Chen, X.; Meng, Y.; Zhang, S.; Ma, X. Iron Nanoparticles Tuned to Catalyze CO2 Electroreduction in Acidic Solutions through Chemical Microenvironment Engineering. *ACS Catal.* **2022**, 7517–7523.
- (15) Louisia, S.; Kim, D.; Li, Y.; Gao, M.; Yu, S.; Roh, I.; Yang, P. The Presence and Role of the Intermediary CO Reservoir in Heterogeneous Electroreduction of CO2. *Proc. Natl. Acad. Sci.* **2022**, *119*, No. e2201922119.
- (16) Seh, Z. W.; Kibsgaard, J.; Dickens, C. F.; Chorkendorff, I.; Nørskov, J. K.; Jaramillo, T. F. Combining Theory and Experiment in Electrocatalysis: Insights into Materials Design. *Science* **2017**, *355*, No. eaad4998.

- (17) Deng, B.; Huang, M.; Zhao, X.; Mou, S.; Dong, F. Interfacial Electrolyte Effects on Electrocatalytic CO2 Reduction. *ACS Catal.* **2022**, *12*, 331–362.
- (18) Bui, J. C.; Kim, C.; King, A. J.; Romiluyi, O.; Kusoglu, A.; Weber, A. Z.; Bell, A. T. Engineering Catalyst–Electrolyte Microenvironments to Optimize the Activity and Selectivity for the Electrochemical Reduction of CO2 on Cu and Ag. Acc. Chem. Res. 2022, 55, 484–494.
- (19) Ruggiero, B. N.; Sanroman Gutierrez, K. M.; George, J. D.; Mangan, N. M.; Notestein, J. M.; Seitz, L. C. Probing the Relationship between Bulk and Local Environments to Understand Impacts on Electrocatalytic Oxygen Reduction Reaction. *J. Catal.* **2022**, *414*, 33–43.
- (20) Shih, A. J.; Arulmozhi, N.; Koper, M. T. M. Electrocatalysis under Cover: Enhanced Hydrogen Evolution via Defective Graphene-Covered Pt(111). ACS Catal. 2021, 11, 10892–10901.
- (21) Bard, A. J.; Faulkner, L. R.; White, H. S. Electrochemical Methods: Fundamentals and Applications; John Wiley & Sons, 2022.
- (22) Xin, H.; Wang, H.; Zhang, W.; Chen, Y.; Ji, Q.; Zhang, G.; Liu, H.; Taylor, A. D.; Qu, J. In Operando Visualization and Dynamic Manipulation of Electrochemical Processes at the Electrode-Solution Interface. *Angew. Chem.* **2022**, *61*, No. e2022062.
- (23) Waegele, M. M.; Gunathunge, C. M.; Li, J.; Li, X. How Cations Affect the Electric Double Layer and the Rates and Selectivity of Electrocatalytic Processes. *J. Chem. Phys.* **2019**, *151*, 160902.
- (24) Monteiro, M. C. O.; Dattila, F.; Hagedoorn, B.; García-Muelas, R.; López, N.; Koper, M. T. M. Absence of CO2 Electroreduction on Copper, Gold and Silver Electrodes without Metal Cations in Solution. *Nat. Catal.* **2021**, *4*, 654–662.
- (25) McEnaney, J. M.; Blair, S. J.; Nielander, A. C.; Schwalbe, J. A.; Koshy, D. M.; Cargnello, M.; Jaramillo, T. F. Electrolyte Engineering for Efficient Electrochemical Nitrate Reduction to Ammonia on a Titanium Electrode. ACS Sustainable Chem. Eng. 2020, 8, 2672–2681.
- (26) Pérez-Gallent, E.; Figueiredo, M. C.; Katsounaros, I.; Koper, M. T. M. Electrocatalytic Reduction of Nitrate on Copper Single Crystals in Acidic and Alkaline Solutions. *Electrochim. Acta* **2017**, 227, 77–84.
- (27) Katsounaros, I.; Kyriacou, G. Influence of the Concentration and the Nature of the Supporting Electrolyte on the Electrochemical Reduction of Nitrate on Tin Cathode. *Electrochim. Acta* **2007**, 52, 6412–6420.
- (28) Yao, Y.; Zhu, S.; Wang, H.; Li, H.; Shao, M. A Spectroscopic Study of Electrochemical Nitrogen and Nitrate Reduction on Rhodium Surfaces. *Angew. Chem.* **2020**, *59*, 10479–10483.
- (29) Bohra, D.; Chaudhry, J. H.; Burdyny, T.; Pidko, E. A.; Smith, W. A. Modeling the Electrical Double Layer to Understand the Reaction Environment in a CO 2 Electrocatalytic System. *Energy Environ. Sci.* **2019**, *12*, 3380–3389.
- (30) Steinmann, S. N.; Michel, C. How to Gain Atomistic Insights on Reactions at the Water/Solid Interface? *ACS Catal.* **2022**, 6294–6301.
- (31) Gu, J.; Liu, S.; Ni, W.; Ren, W.; Haussener, S.; Hu, X. Modulating Electric Field Distribution by Alkali Cations for CO2 Electroreduction in Strongly Acidic Medium. *Nat. Catal.* **2022**, *5*, 268–276.
- (32) Jarvey, N.; Henrique, F.; Gupta, A. Ion Transport in an Electrochemical Cell: A Theoretical Framework to Couple Dynamics of Double Layers and Redox Reactions for Multicomponent Electrolyte Solutions. *J. Electrochem. Soc.* **2022**, *169*, No. 093506.
- (33) Katsounaros, I. On the Assessment of Electrocatalysts for Nitrate Reduction. Curr. Opin. Electrochem. 2021, 28, 100721.
- (34) Resasco, J.; Abild-Pedersen, F.; Hahn, C.; Bao, Z.; Koper, M. T. M.; Jaramillo, T. F. Enhancing the Connection between Computation and Experiments in Electrocatalysis. *Nat. Catal.* **2022**, *5*, 374–381.
- (35) Yan, C.; Kakuturu, S.; Butzlaff, A. H.; Cwiertny, D. M.; Mubeen, S.; Werth, C. J. Scalable Reactor Design for Electrocatalytic Nitrite Reduction with Minimal Mass Transfer Limitations. *ACS EST Eng.* **2021**, *1*, 204–215.
- (36) Abdallah, R.; Geneste, F.; Labasque, T.; Djelal, H.; Fourcade, F.; Amrane, A.; Taha, S.; Floner, D. Selective and Quantitative Nitrate

- Electroreduction to Ammonium Using a Porous Copper Electrode in an Electrochemical Flow Cell. *J. Electroanal. Chem.* **2014**, 727, 148–153
- (37) Zhang, B. A.; Ozel, T.; Elias, J. S.; Costentin, C.; Nocera, D. G. Interplay of Homogeneous Reactions, Mass Transport, and Kinetics in Determining Selectivity of the Reduction of CO2 on Gold Electrodes. ACS Cent. Sci. 2019, 5, 1097–1105.
- (38) Hochfilzer, D.; Xu, A.; Sørensen, J. E.; Needham, J. L.; Krempl, K.; Toudahl, K. K.; Kastlunger, G.; Chorkendorff, I.; Chan, K.; Kibsgaard, J. Transients in Electrochemical CO Reduction Explained by Mass Transport of Buffers. *ACS Catal.* 2022, 5155–5161.
- (39) Jang, J.; Rüscher, M.; Winzely, M.; Morales-Guio, C. G. Gastight Rotating Cylinder Electrode: Toward Decoupling Mass Transport and Intrinsic Kinetics in Electrocatalysis. *AIChE J.* **2022**, *68*, No. e17605.
- (40) Corral, D.; Feaster, J. T.; Sobhani, S.; DeOtte, J. R.; Lee, D. U.; Wong, A. A.; Hamilton, J.; Beck, V. A.; Sarkar, A.; Hahn, C.; Jaramillo, T. F.; Baker, S. E.; Duoss, E. B. Advanced Manufacturing for Electrosynthesis of Fuels and Chemicals from CO2. *Energy Environ. Sci.* 2021, 14, 3064–3074.
- (41) O'Dell, J. W. Determination of Ammonia Nitrogen by Semi-automated Colorimetry. In *Methods for the Determination of Metals in Environmental Samples*; Elsevier, 1996; pp. 434–448, DOI: 10.1016/B978-0-8155-1398-8.50024-0.
- (42) Liu, M. J.; Guo, J.; Hoffman, A. S.; Stenlid, J. H.; Tang, M. T.; Corson, E. R.; Stone, K. H.; Abild-Pedersen, F.; Bare, S. R.; Tarpeh, W. A. Catalytic Performance and Near-Surface X-Ray Characterization of Titanium Hydride Electrodes for the Electrochemical Nitrate Reduction Reaction. *J. Am. Chem. Soc.* 2022, 144, 5739–5744.
- (43) Zhumaev, U. E.; Domke, K. F. Surface-Enhanced Infrared Absorption Spectroscopy. In *Encyclopedia of Interfacial Chemistry*; Wandelt, K., Ed.; Elsevier: Oxford, 2018; pp. 542–548, DOI: 10.1016/B978-0-12-409547-2.13627-3.
- (44) Chen, F.-Y.; Wu, Z.-Y.; Gupta, S.; Rivera, D. J.; Lambeets, S. V.; Pecaut, S.; Kim, J. Y. T.; Zhu, P.; Finfrock, Y. Z.; Meira, D. M.; King, G.; Gao, G.; Xu, W.; Cullen, D. A.; Zhou, H.; Han, Y.; Perea, D. E.; Muhich, C. L.; Wang, H. Efficient Conversion of Low-Concentration Nitrate Sources into Ammonia on a Ru-Dispersed Cu Nanowire Electrocatalyst. *Nat. Nanotechnol.* **2022**, 1–9.
- (45) Dima, G. E.; de Vooys, A. C. A.; Koper, M. T. M. Electrocatalytic Reduction of Nitrate at Low Concentration on Coinage and Transition-Metal Electrodes in Acid Solutions. *J. Electroanal. Chem.* **2003**, 554–555, 15–23.
- (46) Horányi, G.; Rizmayer, E. M. Role of Adsorption Phenomena in the Electrocatalytic Reduction of Nitric Acid at a Platinized Platinum Electrode. *J. Electroanal. Chem. Interfacial Electrochem.* **1982**, 140, 347–366.
- (47) Marcandalli, G.; Monteiro, M. C. O.; Goyal, A.; Koper, M. T. M. Electrolyte Effects on CO2 Electrochemical Reduction to CO. *Acc. Chem. Res.* **2022**, *55*, 1900–1911.
- (48) Wang, H.; Guo, Y.; Li, C.; Yu, H.; Deng, K.; Wang, Z.; Li, X.; Xu, Y.; Wang, L. Cu/CuOx In-Plane Heterostructured Nanosheet Arrays with Rich Oxygen Vacancies Enhance Nitrate Electroreduction to Ammonia. ACS Appl. Mater. Interfaces 2022, 14, 34761–34769.
- (49) Wang, C.; Ye, F.; Shen, J.; Xue, K.-H.; Zhu, Y.; Li, C. In Situ Loading of Cu2O Active Sites on Island-like Copper for Efficient Electrochemical Reduction of Nitrate to Ammonia. *ACS Appl. Mater. Interfaces* **2022**, *14*, 6680–6688.
- (50) Resasco, J.; Chen, L. D.; Clark, E.; Tsai, C.; Hahn, C.; Jaramillo, T. F.; Chan, K.; Bell, A. T. Promoter Effects of Alkali Metal Cations on the Electrochemical Reduction of Carbon Dioxide. *J. Am. Chem. Soc.* **2017**, *139*, 11277–11287.
- (51) Monteiro, M. C. O.; Dattila, F.; López, N.; Koper, M. T. M. The Role of Cation Acidity on the Competition between Hydrogen Evolution and CO2 Reduction on Gold Electrodes. *J. Am. Chem. Soc.* **2022**, *144*, 1589–1602.
- (52) Garlyyev, B.; Xue, S.; Watzele, S.; Scieszka, D.; Bandarenka, A. S. Influence of the Nature of the Alkali Metal Cations on the Electrical

Double-Layer Capacitance of Model Pt(111) and Au(111) Electrodes. J. Phys. Chem. Lett. 2018, 9, 1927–1930.

- (53) Fedurco, M.; Kedzierzawski, P.; Augustynski, J. Effect of Multivalent Cations upon Reduction of Nitrate Ions at the Ag Electrode. J. Electrochem. Soc. 1999, 146, 2569.
- (54) Goyal, A.; Koper, M. T. M. The Interrelated Effect of Cations and Electrolyte PH on the Hydrogen Evolution Reaction on Gold Electrodes in Alkaline Media. *Angew. Chem., Int. Ed.* **2021**, *60*, 13452–13462.
- (55) Yang, K.; Kas, R.; Smith, W. A. In Situ Infrared Spectroscopy Reveals Persistent Alkalinity near Electrode Surfaces during CO2 Electroreduction. *J. Am. Chem. Soc.* **2019**, *141*, 15891–15900.
- (56) Corson, E. R.; Kas, R.; Kostecki, R.; Urban, J. J.; Smith, W. A.; McCloskey, B. D.; Kortlever, R. In Situ ATR-SEIRAS of Carbon Dioxide Reduction at a Plasmonic Silver Cathode. *J. Am. Chem. Soc.* **2020**, *142*, 11750–11762.
- (57) Jackson, M. N.; Jung, O.; Lamotte, H. C.; Surendranath, Y. Donor-Dependent Promotion of Interfacial Proton-Coupled Electron Transfer in Aqueous Electrocatalysis. *ACS Catal.* **2019**, *9*, 3737–3743.
- (58) Da Silva, S.; Basséguy, R.; Bergel, A. Electrochemical Deprotonation of Phosphate on Stainless Steel. *Electrochim. Acta* **2004**, *49*, 4553–4561.
- (59) Marcandalli, G.; Boterman, K.; Koper, M. T. M. Understanding Hydrogen Evolution Reaction in Bicarbonate Buffer. *J. Catal.* **2022**, 405, 346–354.
- (60) Bui, J. C.; Kim, C.; Weber, A. Z.; Bell, A. T. Dynamic Boundary Layer Simulation of Pulsed CO2 Electrolysis on a Copper Catalyst. *ACS Energy Lett.* **2021**, *6*, 1181–1188.
- (61) Chan, K. A Few Basic Concepts in Electrochemical Carbon Dioxide Reduction. *Nat. Commun.* **2020**, *11*, 5954.
- (62) Carvalho, O. Q.; Marks, R.; Nguyen, H. K. K.; Vitale-Sullivan, M. E.; Martinez, S. C.; Árnadóttir, L.; Stoerzinger, K. A. Role of Electronic Structure on Nitrate Reduction to Ammonium: A Periodic Journey. J. Am. Chem. Soc. 2022, 144, 14809–14818.
- (63) Bui, J. C.; Lees, E. W.; Pant, L. M.; Zenyuk, I. V.; Bell, A. T.; Weber, A. Z. Continuum Modeling of Porous Electrodes for Electrochemical Synthesis. *Chem. Rev.* **2022**, *122*, 11022–11084.
- (64) Zhu, X.; Huang, J.; Eikerling, M. PH Effects in a Model Electrocatalytic Reaction Disentangled. *JACS Au* 2023, DOI: 10.1021/jacsau.2c00662.

☐ Recommended by ACS

Recent Advances in Electrocatalytic Nitrate Reduction to Ammonia: Mechanism Insight and Catalyst Design

Yue Cao, Min Luo, et al.

MAY 16, 2023

ACS SUSTAINABLE CHEMISTRY & ENGINEERING

READ 🗹

Pulsed Nitrate-to-Ammonia Electroreduction Facilitated by Tandem Catalysis of Nitrite Intermediates

Panpan Li, Guihua Yu, et al.

MARCH 10, 2023

JOURNAL OF THE AMERICAN CHEMICAL SOCIETY

READ 🗹

Proton Exchange Membrane Electrode Assembly for Ammonia Electrosynthesis from Nitrate

Siqi Li, Quan-Hong Yang, et al.

APRIL 25, 2023

ACS APPLIED ENERGY MATERIALS

READ 🗹

Electrocatalytic NO Reduction to NH₃ on Mo₂C Nanosheets

Kai Chen, Ke Chu, et al.

JANUARY 03, 2023

INORGANIC CHEMISTRY

READ 🗹

Get More Suggestions >